Synergistic Effects in 3D Honeycomb-like Hematite Nanoflakes/Branched Polypyrrole Nanoleaves Heterostructures as High-Performance Negative Electrodes for Asymmetric Supercapacitors

Peng-Yi Tang,[*,†,‡,a] *Li-Juan Han,*[§,a] *Aziz Genç,*[†] *Yong-Min He,*[∥] *Xuan Zhang,*[⊥] *Lin Zhang,*[#] *José Ramón Galán-Mascarós,*[§,▵] *Joan Ramon Morante,*[‡] *and Jordi Arbiol*[*, †, ▵]

[†]Catalan Institute of Nanoscience and Nanotechnology (ICN2), CSIC and The Barcelona Institute of Science and Technology, Campus UAB, Bellaterra, 08193 Barcelona, Spain, [‡]Catalonia Institute for Energy Research (IREC), Jardins de les Dones de Negre 1, Sant Adrià del Besòs, Barcelona 08930, Catalonia, Spain, [§] Institute of Chemical Research of Catalonia (ICIQ), The Barcelona Institute of Science and Technology, Avinguda Paisos Catalans 16, Tarragona 43007, Catalonia, Spain, [∥]School of Physical Science and Technology, Lanzhou University, Lanzhou 730000, People's Republic of China, [⊥]Department of Materials Science (MTM), KU Leuven, Leuven 3001, Belgium, [#]Department of Integrated System Engineering, The Ohio State University, Columbus, OH 43210 U.S.A, [▵]Institució Catalana de Recerca i Estudis Avançats (ICREA), Passeig Lluis Companys, 23, E-08010, Barcelona, Spain.

*Corresponding Authors.

E-mail address: tpy965421@gmail.com, ptang@irec.cat (Pengyi Tang); arbiol@icrea.cat (Jordi Arbiol).

Author Contributions. [a] These authors contributed equally.

Abstract

Rational assembly of unique branched heterostructures is one of the facile techniques to improve the electrochemical figure of merit of materials. By taking advantages of hydrogen bubbles dynamic template, hydrothermal method and electrochemical polymerization, branched polypyrrole (PPy) nanoleaves decorated honeycomb-like hematite nanoflakes (core-branch Fe_2O_3@PPy) are fabricated. X-ray diffraction, X-ray photoelectron spectroscopy, scanning electron microscopy, transmission electron microscopy (TEM), high-resolution TEM, and scanning transmission electron microscopy in high angle annular dark field mode with electron energy loss spectroscopy were combined to elucidate the mechanisms underlying formation and morphogenesis evolution of core-branch Fe_2O_3@PPy heterostructures. Benefiting from the stability of honeycomb-like hematite nanoflakes and the high conductivity of PPy nanoleaves, the resultant core-branch Fe_2O_3@PPy exhibits an ultrahigh capacitance of 1167.8 F g^{-1} at 1A g^{-1} in 0.5 M Na_2SO_4 aqueous solution. Moreover, the assembled bi-metal oxides asymmetric supercapacitor (Fe_2O_3@PPy//MnO_2) gives rise to a maximum energy density of 42.4 Wh kg^{-1} and a maximum power density of 19.14 kW kg^{-1} with an excellent cycling performance of 97.1% retention after 3000 cycles at 3 A g^{-1}. These performance features are superior than previous reported iron oxide/hydroxides based supercapacitors, offering an important guideline for future design of advanced next-generation supercapacitors.

Keywords

Fe_2O_3; PPy; synergistic effects; negative electrode; core-branch

Introduction

Supercapacitors, bridging the gap between high energy batteries and high power dielectric capacitors, have been regarded as an important class of energy storage devices for high power supplies, electric and hybrid vehicles, and portable electronics [1]. Typically, the energy density (E, Wh kg^{-1}) of supercapacitors depends on the cell potential (V) and specific capacitance (C_{sp}, F g^{-1}), $E=2^{-1} C_{sp}V^2$ [2-6]. Due to the limited cell potential (e.g. the value of commercial MAWELL capacitors is ca. 0.7 V) [4], the energy density of conventional symmetrical supercapacitors is much lower in comparison to that delivered by batteries. In such a case, asymmetrical supercapacitors (ASCs) with wider cell potential came into being, which basically are made up of a battery-type Faradaic positive electrode (as the energy source) and a double-layer-type negative electrode (as the power source) [5-7]. Up to date, various metal oxides and conductive polymers have been extensively investigated as positive electrodes, [8-9] coupling with negative electrodes, like carbon sheets [10], activated carbon (AC) [11], carbon nanotubes (CNTs) [12], and graphene [13-14] for possible application in high-performance ASCs. Advances in this prototype have yielded ASCs with good power density; whilst, the low specific capacitance of carbon materials (maximum ca. 300 F g^{-1}) severely limits their energy density [15-18]. In order to push the energy-density limit of ASCs, the exploration of alternative, state-of-the-art negative electrodes with higher capacitance than carbon materials is highly valuable and significant.

Recently, some emerging transition metal oxides or sulfides, such as V_2O_5 [19], V_3S_4 [20], In_2O_3 [21], MoO_3 [22], and Co_9S_8 [23] as negative electrodes for ASCs application have drawn attention of researchers. Hematite (α-Fe_2O_3) is one of the most promising candidates because of its large theoretical specific capacitance (3265 F g^{-1} for the voltage window of -1.0 V-0 V), suitable working window, low cost, abundance, and non-toxicity [9, 24]. However, the practical

implementation of Fe_2O_3 based negative electrodes was prevented by its poor electrical conductivity ($\sim 10^{-14}$ S/cm) [25]. To tackle the limitation and improve its electrochemical performance, great efforts have been made to construct nanostructured Fe_2O_3, like oxygen-deficient nanorods [9], nanoflowers [25], nanowires [26], and nanoneedles [27]. Other researchers alternatively combined Fe_2O_3 with highly conductive materials such as CNTs [28], graphene [29-31] and poly (3, 4-ethylenedioxythiophene) (PEDOT) [6] by taking advantages of the excellent conductivity of carbon or conductive polymer species. For example, X. H. Lu et al. designed a Ti-Fe_2O_3@PEDOT core-shell electrode, showed a relatively high specific capacitance of 311.6 F g^{-1} at 1 mA cm^{-2} with superior cycling durability and more than 96% capacitance retention after 30,000 cycles [6]. But nonetheless, the obtained specific capacitance (~9.5%) is far lower than the theoretical specific capacitance and it enhanced the life cycle by sacrificing its energy density,[6] which is expected to be improved via designing three-dimensional (3D) branched nanoarchitectures self-aligned on the substrate [32].

Compared with 0D nanoparticles, 1D nanowires and 2D nanosheets, 3D branched nanoarchitectures possess extraordinary advantages, including structural hierarchy, higher surface areas and direct electron and ion transport pathways, and thus holds great promise on the functionality of composite for various application fields, like solar cell, water splitting, lithium-ion batteries and supercapacitors etc [32-35]. In spite of these merits, for batteries and supercapacitors application, controlling the size, dimension, and composition of the building blocks of branched nanostructures in an expected manner, and maintaining their structure stability and good electrical conductivity during repeated cycling are still great challenges [32]. On the other hand, B. A. Lu et al. reported that the honeycomb-like $CoMoO_4$ (96.3% capacitance retention) was more stable than $CoMoO_4$ with nanowires (74.14% capacitance retention) and

nanosheets (84.69% capacitance retention) structure during a continuous life cycling for 1000 times at 15.71 A g^{-1} [36]. With this in mind, honeycomb-like matrix using as the backbone of branched nanoarchitectures to form core-branch nanostructure may further boosts their cycle life. Meanwhile, PPy species serving as a protective shell of metal oxides (like layered double hydroxide [16], MnO_2 [37], and MoS_2 [38] forming core-shell nanostructures have been evidenced to be a powerful tool for effectively improving the electrochemical behavior of positive electrodes. Further, C. Debiemme-Chouvy et al.'s report about the fabrication of well-defined PPy nanowires on Au film through simple electropolymerization by exerting control over the weak-acidic and non-acidic anions content in the deposition electrolyte sheds light to construct high conductive ordered branch structure on backbone matrix [39-40]. In fact, researches combining the merits of stability of honeycomb-like matrix (metal oxides) on the ion transportation and the superiority of branch structure (conductive polymers) on the electron transferring are still scarce, to saying nothing of reports elucidating the mechanisms underlying formation and morphogenesis evolution of core-branch nanostructure to extract design principles that may enable the conductive polymer formation on other metal oxides with similar capabilities.

Herein, for the first time, we synthesized a core-branch honeycomb-like Fe_2O_3 nanoflakes@PPy nanoleaves arrays grown on three-dimensional nickel foam (NF) scaffold, comprising one-dimensional (1-D) leaves-like PPy, 2-D mesoporous Fe_2O_3 nanoflakes, and 3-D macroporous NF, as displayed in Schematic 1 and thoroughly investigated the formation mechanism of branched PPy nanoleaves. The as-prepared core-branch Fe_2O_3@PPy electrode shows a remarkably large specific capacitance of 1167.8 F g^{-1} at 1 A g^{-1} with a good rate capability. To the best of our knowledge, these are the best specific capacitance values ever reported for iron oxides/hydroxides based electrodes (see the comparison in Table S1).

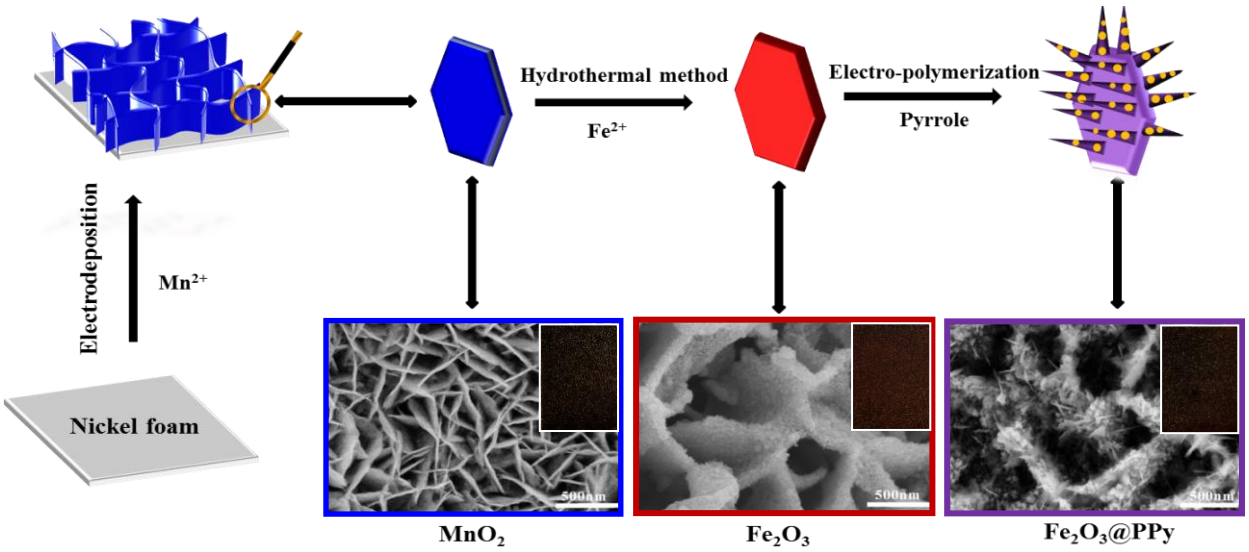

Schematic 1 Fabrication process of core-branch Fe_2O_3@PPy heterostructures (the insets show the digital photographs of MnO_2, Fe_2O_3 and Fe_2O_3@PPy electrodes).

Experimental Section

Synthesis of MnO_2 nanosheets on nickel foam (NF): The MnO_2 nanosheets were synthesized by a cathode electrodeposition technology in a three-electrode system according to Liu et al.'s report [41-42]. By employing cathodic electrodeposition, MnO_2 nanosheets were deposited on NF (active area: 1.5 cm× 2 cm; thickness: 1.8 mm, pore density: 110 ppi, Changsha Liyuan New Material), which was first cleaned by acetone and deionized water. Platinum (Pt) plate and saturated calomel electrode (SCE) were served as the counter and reference electrodes, respectively; and 0.02 M manganese acetate and 0.02 M sodium sulfate aqueous solution worked as the electrolyte. The electrodeposition of MnO_2 on NF substrate was carried out at a constant potential of -1.6 V for 150 s. After that, the obtained sample was rinsed in deionized water for several times and then it was dried at 200 °C for 2 h.

Synthesis of honeycomb-like Fe_2O_3 nanoflakes on NF: The obtained MnO_2 nanosheets sample was employed as the sacrificed template to synthesize the honeycomb-like Fe_2O_3 nanoflakes by a

previously reported method with slight modifications [43]. And the detail process is as following: Then, 21 mg of $FeSO_4 \cdot 7H_2O$ (Aladdin, 99.9 %) was dissolved in 30 mL of mixed ethylene glycol and deionized water (v/v = 1/7). After stirring for about 10 min, this translucent solution and the as-prepared MnO_2 nanoflakes on NF were both transferred into a 50 mL Teflon-lined stainless steel autoclave, followed by heating at 120 ^oC for 0.5 h in an electric oven. After heating, the autoclave was cooled naturally to room temperature. The nickel foam with iron hydroxides were obtained due to the following reaction during the hydrothermal process (equation 1 and 2),

$$[Fe(H_2O)_6]^{2+} \rightarrow [Fe(OH)(H_2O)_5]^{+} + H^{+} \quad (1)$$

$$2Fe^{2+} + MnO_2 + 4H^{+} \rightarrow 2Fe^{3+} + Mn^{2+} + 2H_2O \quad (2)$$

$$[Fe(H_2O)_6]^{3+} \rightarrow Fe(OH)_3(s) + 3H^{+} + 3H_2O \quad (3)$$

Then, the samples were taken out and rinsed thoroughly with absolute ethanol and dried at room temperature. The honeycomb-like α-Fe_2O_3 nanoflakes were obtained by annealing the as-prepared iron hydroxide product at 400 ^oC in air for 2 h with a heating rate of 2 ^oC min^{-1} (equation 3).

Synthesis of PPy nanoleaves decorated honeycomb-like hematite nanoflakes on NF: Afterwards, the aforementioned honeycomb-like Fe_2O_3 nanoflakes on NF were worked as the working electrode for the deposition of PPy nanoleaves. The PPy species were deposited at a constant potential of 1.0 V vs SCE. in the medium aqueous of 80 mM pyrrole, 100 mM $LiClO_4$, and 140 mM sodium dodecyl sulfate. Finally, the obtained sample was washed with deionized water several times, and then it was dried at 60 °C. The mass of PPy shell and core Fe_2O_3 species was determined by a high-precision microbalance with sensitivity of 0.1 mg.

Assembly of an ASC: For the construction of an asymmetric supercapacitor device, MnO_2

nanosheets and core-branch Fe_2O_3@PPy and piece of commercial supercapacitor separator membrane (DR2012, thickness: 0.12 ± 0.01mm, Suzhou Beige New Materials & Technology Co. Ltd..) were used as the positive, the negative electrodes and separator, respectively (as shown in the inset of Figure 5D). And the electrodes, 0.5 M Na_2SO_4 and separator were enveloped in aluminium plastic bags. The mass ratio of negative electrode to positive electrode was calculated based on charge balance theory according to the electrochemical data shown in Figure S11 and 12.

Microstructural Properties Characterization: The as-synthesized samples were characterized using X-ray powder diffraction (XRD; Rigaku RU-300 diffractometer; monochromated Cu Kα1 radiation, λ = 1.540 598 1 Å; 60.0 kV, 30.0mA), field emission scanning electron microscope (SEM, 5.0 kV, SU-8010, Hitai), transmission electron microscopy (TEM, 200kV, Tecnai F20, FEI), scanning transmission electron microscopy-electron energy loss spectroscopy (STEM-EELS, 200 kV under a high angle annular dark field (HAADF), Tecnai F20, FEI). Energy dispersive X-ray spectrometer (EDS), X-ray photoelectron spectroscopy (XPS, Escalab 250Xi) and Raman Spectrum (incident wavelength: 514 nm, InVia-RENISHAW).

Electrochemical Properties Measurement: The electrochemical performance of MnO_2 nanosheets and core-branch Fe_2O_3@PPy electrodes and the corresponding asymmetric supercapacitor was characterized by CV, GCD, and EIS (recorded at open circuit potential with amplitude of 5 mV in the frequency range of 10^{-2}-10^5 Hz) techniques on a CHI 760E electrochemical workstation at ambient temperature. All the measurements were carried out in a 0.5 M Na_2SO_4 aqueous solution. In the three-electrode system, a Pt plate of 2.0 cm × 2.0 cm and a SCE were applied as the counter and reference electrodes, respectively. The specific capacitance measured by chronopotentiometry was calculated according to the equation as

follows:

$$C_{sp} = I \times \Delta t / (\Delta V \times m) \quad (4)$$

where C_{sp} (F g^{-1}) is the specific capacitance of the electrode ($C_{sp\text{-}e}$) or ASC ($C_{sp\text{-}a}$), I (A) is the constant discharging current, Δt (s) is the discharging time, ΔV (V) is the voltage change excluding IR drop at a constant discharge current, and m (g) is the active material mass of a single electrode or the total active material mass of positive and negative electrodes.

For the two-electrode configuration, the energy (E, Wh kg^{-1}) and power densities (P, kW kg^{-1}) were calculated by using the following equations:

$$E = \frac{C_{sp-d} \Delta V^2}{2}, P = \frac{\Delta V I}{2m} \quad (5)$$

where $C_{sp\text{-}d}$ (F g^{-1}), ΔV (V), I (A) and m (g) are the specific capacitance of the asymmetric supercapacitor, the voltage change excluding IR drop at a constant discharge current, discharging current and the total active material mass of positive and negative electrodes, respectively.

Results and discussion

The composition, structure, and morphology of as-prepared samples were investigated by different characterization techniques including X-ray diffraction (XRD), X-ray photoelectron spectroscopy (XPS), scanning electron microscopy (SEM), transmission electron microscopy (TEM), high-resolution TEM (HRTEM), and a combination of scanning transmission electron microscopy (STEM) in high angle annular dark field (HAADF) mode with electron energy loss spectroscopy (EELS).

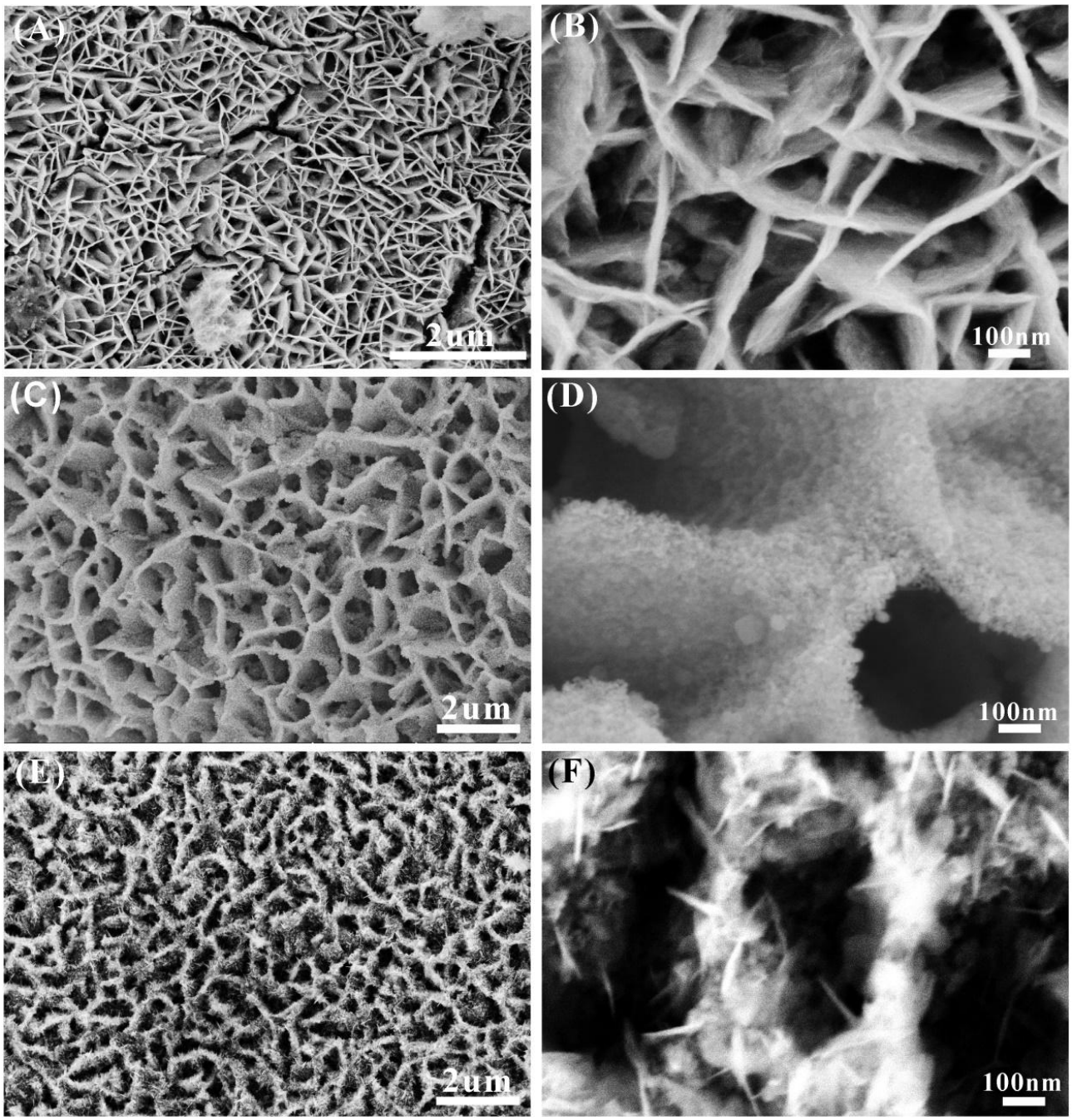

Figure 1. SEM images of MnO_2 nanosheets (A-B), honeycomb-like Fe_2O_3 nanoflakes (C-D) and honeycomb-like Fe_2O_3 nanoflakes@PPy nanoleaves (E-F).

As shown in Figure 1A and B, quasi-vertical MnO_2 nanosheets were first grown on NF through hydrogen bubbles dynamic template induced by an externally applied voltage of -1.6 V [41-42]. And then, the obtained MnO_2 nanosheets worked as the sacrificed template for the subsequent

growth of Fe_2O_3 species through hydrothermal methods. From 1C, it is clear that the honeycomb-like Fe_2O_3 in the form of a seamless interconnected network comprised of ordered oriented nanoflakes almost replicated the morphology of MnO_2 nanosheets without collapsing and cracking. High magnification SEM in Figure 1D reveals that Fe_2O_3 nanoflakes are composed of numerous nanoparticles. The EDS in Figure S1 confirms that all MnO_2 species in nanosheets have been converted to Fe_2O_3 species. Additionally, the honeycomb-like Fe_2O_3 nanoflakes at various reaction stages were presented in the Figure S2 by setting the reaction time, demonstrating the importance of controlling the reaction time of hydrothermal process. PPy species were successfully deposited onto the wall of Fe_2O_3 nanoflakes by further electrochemical polymerization, as displayed in Figure 1E. High magnification image in Figure 1F confirms that the Fe_2O_3 nanoflakes were fully wrapped by PPy nanoleaves with a length of ca. 100 nm to form Fe_2O_3@PPy core-branch arrays, which provides a large interfacial area for reaction, and numerous channels for rapid diffusion of electrolyte ions as discussed below. Moreover, to optimize the functionality of the structure of Fe_2O_3@PPy, the parallel experiment in terms of controlling the deposition of PPy was also conducted (Figure S3). As the electrochemical polymerization proceeded, the PPy nanoleaves grew into locally jammed structure, which not only blocks the electrolyte ion accessibility but also may deteriorate their electrochemical performance.

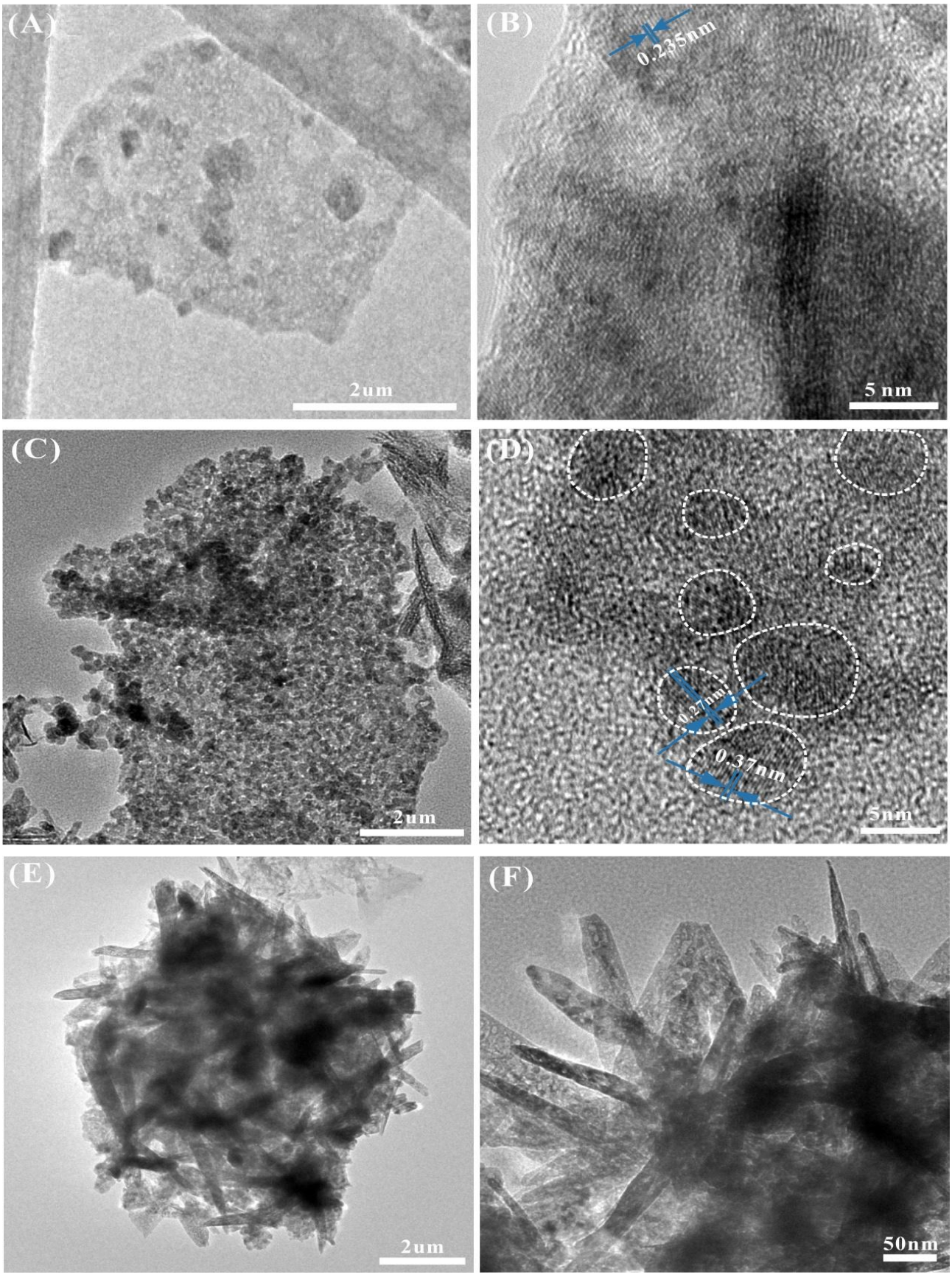
(A)
2um
(B)
0.235nm
5 nm
(C)
2um
(D)
0.27nm
0.37nm
5nm
(E)
2um
(F)
50nm

Figure 2. TEM images of MnO_2 nanosheets (A-B), honeycomb-like Fe_2O_3 nanoflakes (C-D) and honeycomb-like Fe_2O_3 nanoflakes@PPy nanoleaves (E-F).

The nanosheets structure of MnO_2 sample was further confirmed by TEM inspection as shown in Figure 2A. And Figure 2B reveals that the interplanar spacing is ca. 0.235 nm, which is indexed to ε-MnO_2 (JCPDF#12-0141) [41-42]. The resultant Fe_2O_3 nanoflake (Figure 2C) is made of a large variety of small nanopartices with diameter from 2 nm to 6 nm, and thus presents a mesoporous structure in the plane of nanoflakes. The well-resolved lattice fringes with spacing of 0.27 nm and 0.37 nm shown in Figure 2D correspond to the distance between (104) and (012) planes for α-Fe_2O_3 (JCPDS NO. 33-0664) [6, 44-45]. Moreover, PPy nanoleaves strongly coupled with mesoporous Fe_2O_3 nanoflakes forming a homogenous structure, as proved by Figure 2E. Additionally, there are no exposed Fe_2O_3 nanoparticles, further demonstrating the mesoporous Fe_2O_3 nanoflakes were well wrapped by PPy nanoleaves (Figure 2F).

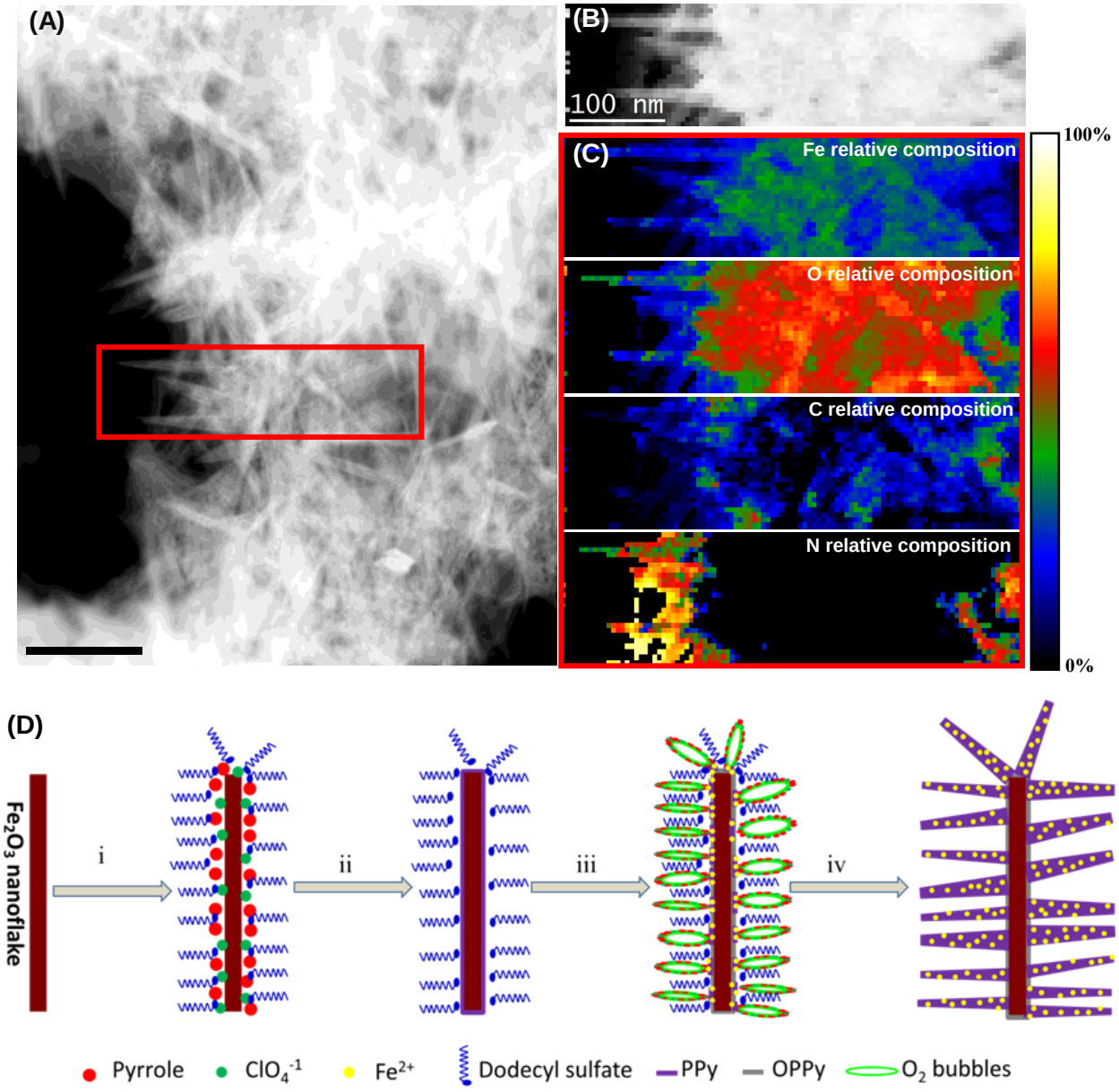

Figure 3. STEM-EELS chemical composition maps of core-branch Fe_2O_3@PPy obtained from the red-rectangle area shown in the STEM micrograph (A), simultaneously obtained HAADF STEM micrograph (B) and relative compositions (C) of Fe, O, C and N (The scale bar is the same for all composition maps). (D) Schematic illustrates the formation mechanism of PPy nanoleaves on Fe_2O_3 nanoflakes, Step (i): immersing Fe_2O_3 nanoflakes in the solution of aqueous of 80 mM pyrrole, 100 mM $LiClO_4$, and 140 mM sodium dodecyl sulfate, Step (ii): Electrodeposition of an ultrathin PPy film on Fe_2O_3 nanoflakes when applied a high potential of

1.0V vs. SCE, Step (iii): Generation of OH^- which overoxidizes PPy, Step (iv): Further electropolymerization growth of the PPy species

To precisely figure out the composition in the nanoleaves and nanoflakes of core-branch Fe_2O_3@PPy, STEM-HAADF and STEM-EELS have been conducted, as displayed in Figure 3. Figure 3A and B correspond to the HAADF STEM images of the core-branch Fe_2O_3@PPy, showing a general view and a magnified detail, respectively. The relative compositions of Fe, O, C and N elements in the nanoflakes and nanoleaves region (Figure 3C) have been mapped by means of EELS analysis using Hartree-Slater model for signal quantification and power law for background removal. The elemental relative composition maps suggest a fairly homogeneous distribution of Fe and O throughout the nanoflakes. Specifically, the Fe and O elements at nanoflakes region have a relative composition of ~35 ± 4 at% and 60 ± 5 at %, which is almost equal to the nominal compositions of the Fe_2O_3 phase (Fe: 40 %, O: 60 %); whilst these values at nanoleaves regions are ~20 ± 4 at % and 25 ± 5 at %, which is nearly equal to the nominal compositions of the FeO phase (Fe: O=1:1). These results reveal that the Fe_2O_3 content dominates the nanoflakes region, while FeO phase is mainly located at the nanoleaves region. Meanwhile, the signals of C and N elements is relatively weak at the center of nanoflakes, indicating there could be only an extremely thin PPy film on the surface plane of Fe_2O_3 nanoflakes. However, the elemental relative compositions of C and N at the nanoleaves regimes are 25 ± 5 at%, and 45 ± 5 at%, indicating that PPy species dominate the nanoleaves region. Furthermore, in concordance with analysis of elemental relative composition of the well-retained Fe_2O_3@PPy core-branch region, the XRD (Figure S4), XPS (Figure S5), Raman Spectrum (Figure S6) and EELS mapping analysis (Figure S7) of flaking debris unambiguously concur the formation of the core-branch structure.

Furthermore, in Figure S8, the I (t) response curves of PPy electropolymerization in this case are similar to pyrrole (Py) deposited in the weak-acidic and non-acidic anions, which results in the formation of well-defined PPy nanowires on Au film [39-40]. Thus, the deposition of branched PPy on Fe_2O_3 nanoflakes may follow a possible mechanism shown in Schematic S1. However, the EELS map and relative composition analyses evidence that Fe element penetrates in the form of FeO into the region where the PPy nanoleaves exist. Based on these results, the formation process of the PPy nanoleaves on Fe_2O_3 naoflakes is proposed in Figure 3D. Step (i): the obtained Fe_2O_3 nanoflakes immersed in the solution of aqueous of 80 mM pyrrole, 100 mM $LiClO_4$, and 140 mM sodium dodecyl sulfate (SDS). Due to the inducing covalent bonding between the Fe^{3+} and the partial negative charge of the N atom in the Py structure, dodecyl sulfate and ClO_4^{-1} ions, these anions are absorbed on the wall of nanoflakes. Specifically, ClO_4^{-1} ion was closed to the Fe_2O_3 nanoflakes, whereas the dodecyl sulfate of SDS was relatively far away from the Fe_2O_3 nanoflakes because of its long chain structure of alkyl.

Step (ii): Electrodeposition of an ultrathin PPy film on Fe_2O_3 nanoflakes when applied a high potential of 1.0V vs. SCE. The oxidation of pyrrole (Py) leads to the formation of a thin polypyrrole under its oxidized form on the surface of Fe_2O_3 nanoflakes, form doped with anions (ClO_4^-), according to the following reaction [39]:

$$\mathrm{nPy} + \gamma\mathrm{nClO_4}^- \rightarrow \left[(\mathrm{Py})_\mathrm{n}{}^{(\gamma\mathrm{n})^+}, \gamma\mathrm{nClO_4}^-\right] + 2(\mathrm{n}-1)\mathrm{H}^+ + \left((2+\gamma)\mathrm{n}-2\right)\mathrm{e}^- \quad (6)$$

where γ stands for the doping level of the polymer, it generally ranges from 0.25 to 0.33.

$$\mathrm{H_2O} \rightarrow \mathrm{OH}\cdot + \mathrm{H}^+ + \mathrm{e}^- \quad (7)$$

$$\mathrm{PPy(ClO_4)} + \mathrm{OH}\cdot \rightarrow \mathrm{OPPy} + \mathrm{HClO_4} + \cdots \quad (8)$$

$$2\mathrm{OH}\cdot \rightarrow \mathrm{H_2O_2} \quad (9)$$

$$\mathrm{H_2O_2} \rightarrow \mathrm{O_2} + 2\mathrm{H}^+ + 2\mathrm{e}^- \quad (10)$$

$$Fe_2O_3 + 6H^+ \rightarrow Fe^{3+} + H_2O \quad (11)$$

Step (iii): Generation of $OH^{\cdot}$ which overoxidizes PPy (OPPy) based on the equations (2) and (3). Since hydroxyl radical can also react with itself leading to H_2O_2 that is further oxidized to O_2, the produced O_2 nanobubbles will protect partial PPy species against the action of $OH^{\cdot}$, according to equations of (9) and (10). And the byproduct H^+ around the interface of Fe_2O_3 and O_2 bubbles make the Fe_2O_3 on the surface of nanoflakes region into Fe^{3+} ion due to the localized low pH value, can be up to 1 (equations 11) [40].

$$n\mathrm{Fe}^{3+} + 2\mathrm{nPy} \rightarrow 2\mathrm{nH}^+ + \mathrm{PPy} + \mathrm{nFe}^{2+} \quad (12)$$

Step (iv): Further electropolymerization (equation 1) growth of the PPy species based on the template composed of O_2 nanobubbles and dodecyl sulfate, finally leading to the formation of PPy nanowires. At the same time, the induced Fe^{3+} ions diffuse into the electrolyte and favorably bind with the nitrogen-containing groups on PPy nanoleaves via complexation and electrostatic interactions [29]. During the subsequent electrochemical growth stage of PPy nanowires, Fe^{3+} elements interact with Py species inside the nanowires region, simultaneously forming a microcell for chemical polymerization (equations 12), which results in leave-like PPy nanowires with conical shape because of the Fe^{3+} gradient in the growth direction of PPy nanowires. And then the subsequent heat treatment in air enables the transformation of the doped Fe^{2+} in the PPy nanoleaves into FeO species. Indeed, the doping of Fe element into PPy regime through electrostatic interaction is analogous to the carbonization of iron ions adsorbed onto polyaniline nanosheet/graphene oxide hybrid material reported by Z.J. Fan et al [29].

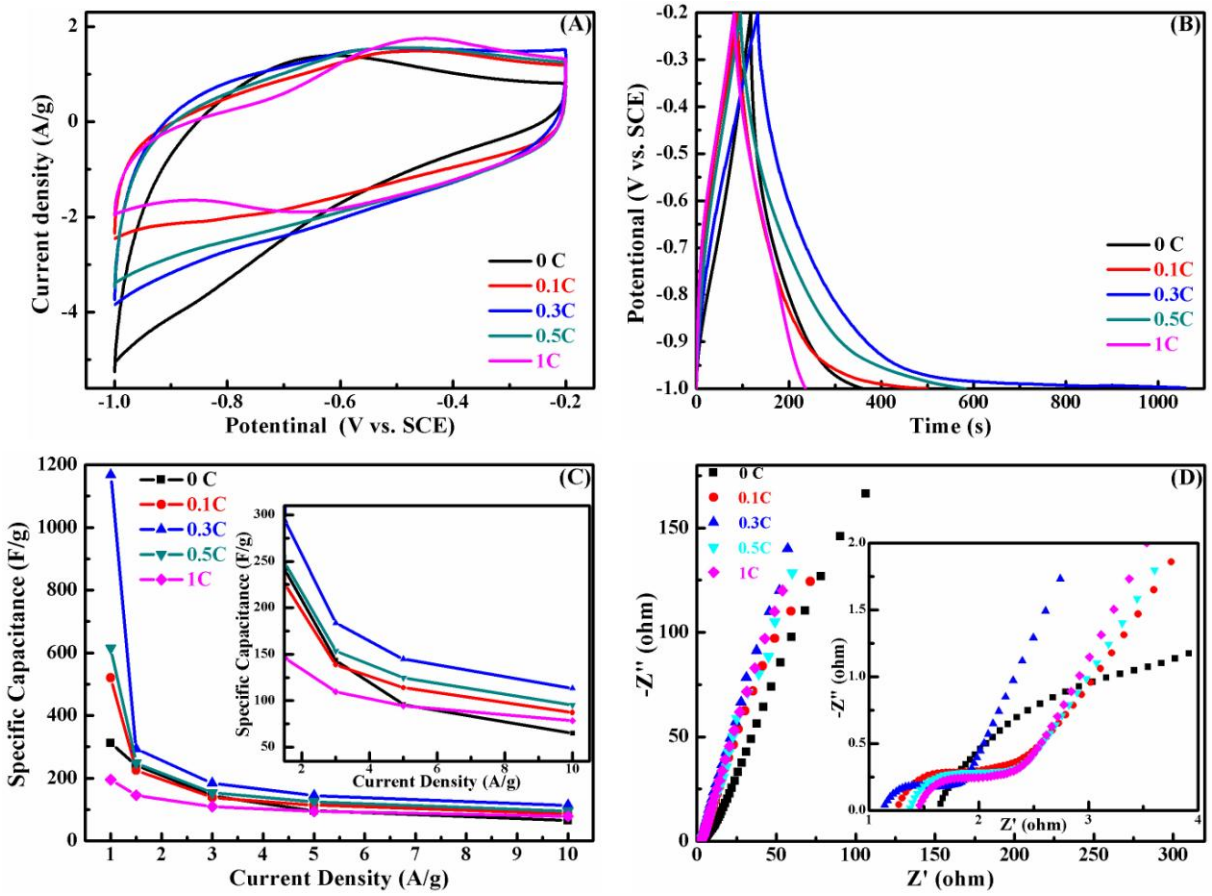

Figure 4. The electrochemical properties of Fe_2O_3 and core-branch Fe_2O_3@PPy with different PPy deposition charges: (A) CV curves at 10 mV s^{-1}, (B) GCD at 1A g^{-1}, (C) the relationship between specific capacitance and current density and (D) the Nyquist diagrams.

As a proof-of-concept demonstration of the function of core-branch Fe_2O_3@PPy, the cyclic voltammetry (CV), galvanostatic charge-discharge (GCD), rate capabilities and electrochemical impedance spectroscopy (EIS) were performed in a three-electrode electrochemical cell, as displayed in Figure 4. The CV curve of α-Fe_2O_3 have one pair of redox peaks, involving the Fe^{2+}/Fe^{3+} redox couple and probably mediated by the Na^+ ions in the neutral electrolyte. When scanned to the negative potential direction, Fe^{3+} is reduced to Fe^{2+} with a peak at about -1.05 V vs. (Hg/HgO) [31]. To avoid the appreciable hydrogen evolution, in this work, the CV curves of all Fe_2O_3 based electrodes were cycled from -1 V to -0.2 V vs. SCE. Typically, Fe^{2+} is oxidized

to Fe^{3+} when scanned to the positive direction, consistent with the oxidation peak observed at ca. -0.6 V vs. SCE. in CV of Fe_2O_3 nanoflakes electrode, as shown in Figure 4A [31]. With the increasing of PPy deposition, the CVs of Fe_2O_3@PPy electrodes exhibit quasi-rectangular shape, indicating their reversible performance. When the PPy deposition reached 1.0 C, another pair of peaks appears which can be assigned to doping/unhoping process between PPy and Na^+ for charge storage. And the redox peaks of Fe_2O_3 almost disappear probably because of the shielding effectiveness of the over-deposited PPy species (Figure S3D). Among these core-branch electrodes, the Fe_2O_3@PPy electrode with 0.3C PPy deposition (donated as Fe_2O_3@PPy-0.3C) possesses the largest integral area as well as the maximum current response per unit. Moreover, even at a scan rate of 500 mV s^{-1} (Figure S9), the CV profile still maintains a quasi-rectangular, revealing its good rate characteristics. Figure 4B reveals that the Fe_2O_3@PPy-0.3C possesses the longest discharge time at a current density of 1 A g^{-1}, which is consistent with the aforementioned CV results. [46] According to Figure 4C and Figure S10 A, with the increment of PPy deposition charges, the specific capacitance of Fe_2O_3@PPy core-branch nanoflakes increases at the beginning to a maximum (1167.8 F g^{-1} at 1 A g^{-1}) at 0.3 C PPy deposition, which is much higher than that of the pristine Fe_2O_3 nanoflakes electrode (312.5 F g^{-1} at 1 A g^{-1}) and those reported previously about iron oxides/hydroxides based electrodes (Table S1). Even considering the quasi-linear part of GCD, the specific capacitance of the optimized Fe_2O_3@PPy core-branch nanoflakes (405.5 F g^{-1}) is still higher than that of pristine Fe_2O_3 nanoflakes (265.3 F g^{-1}), as shown in Figure S10 C and D. These results further demonstrate the great advantages of core-branch structure of Fe_2O_3@PPy. Afterwards it decreases upon further increment of PPy deposition because the overloaded PPy (see the SEM in Figure S3 C and D of 0.5 C and 1.0 C PPy deposition) hinders the electrolyte ions from penetrating into the pore of Fe_2O_3 nanoflakes.

Moreover, rate capability is one of the important factors in evaluating the power application of supercapacitors as well. The GCD profiles of the pristine Fe_2O_3 and Fe_2O_3@PPy electrodes at different current densities were measured. From the inset of Figure 4C, the pristine Fe_2O_3 electrode shows a specific capacitance of 65.0 F g^{-1} at 10 A g^{-1}. The Fe_2O_3@PPy-0.3C electrode, by contrast, still maintains a specific capacitance as high as 113.4 F g^{-1} [47]. The enhanced capacitance and rate capability of the Fe_2O_3@PPy-0.3C electrode can be attributed to the improvement of electrical conductivity of the electrode after coating with the optimized PPy nanoleaves. The fast ion diffusion kinetics and effective electron transfer rate in the Fe_2O_3@PPy nanoflakes electrode are further confirmed by the EIS in Figure 4D. The impedance at high frequency (100 kHz) reflects the equivalent series resistance (ESR) in the electrode/electrolyte system, which is related to the electrical conductivity of the electrode [48-49]. The ESR of pristine Fe_2O_3 and core-branch Fe_2O_3@PPy electrodes with 0.1, 0.3, 0.5 and 1.0 C PPy deposition charges is 1.65, 1.27, 1.14, 1.37 and 1.46 Ω, together with the reduced slop of IR drop of core-branch Fe_2O_3@PPy-0.3C electrode shown in Figure S10B, concurring the best conductivity of the core-branch Fe_2O_3@PPy-0.3C electrode. In addition, the semicircle of the Nyquist diagram corresponds to the faradaic reactions, its diameter represents the interfacial charge-transfer resistance (R_{ct}), and the linear part corresponds to the Warburg impedance, which is described as a diffusive resistance of electrolyte into the electrode pores [50]. The R_{ct} of Fe_2O_3@PPy-0.3C electrode is the lowest one among these electrodes and the highest slope at low frequency part demonstrates its superior ion diffusion ability than other electrodes. The results concur that the combination of high electrical conductivity pathways for charge transfer derived from the coating of PPy nanoleaves as well as fast ion diffusion kinetics result from honeycomb-like Fe_2O_3 is responsible for the excellent electrochemical performance of Fe_2O_3@PPy-0.3C

electrode.

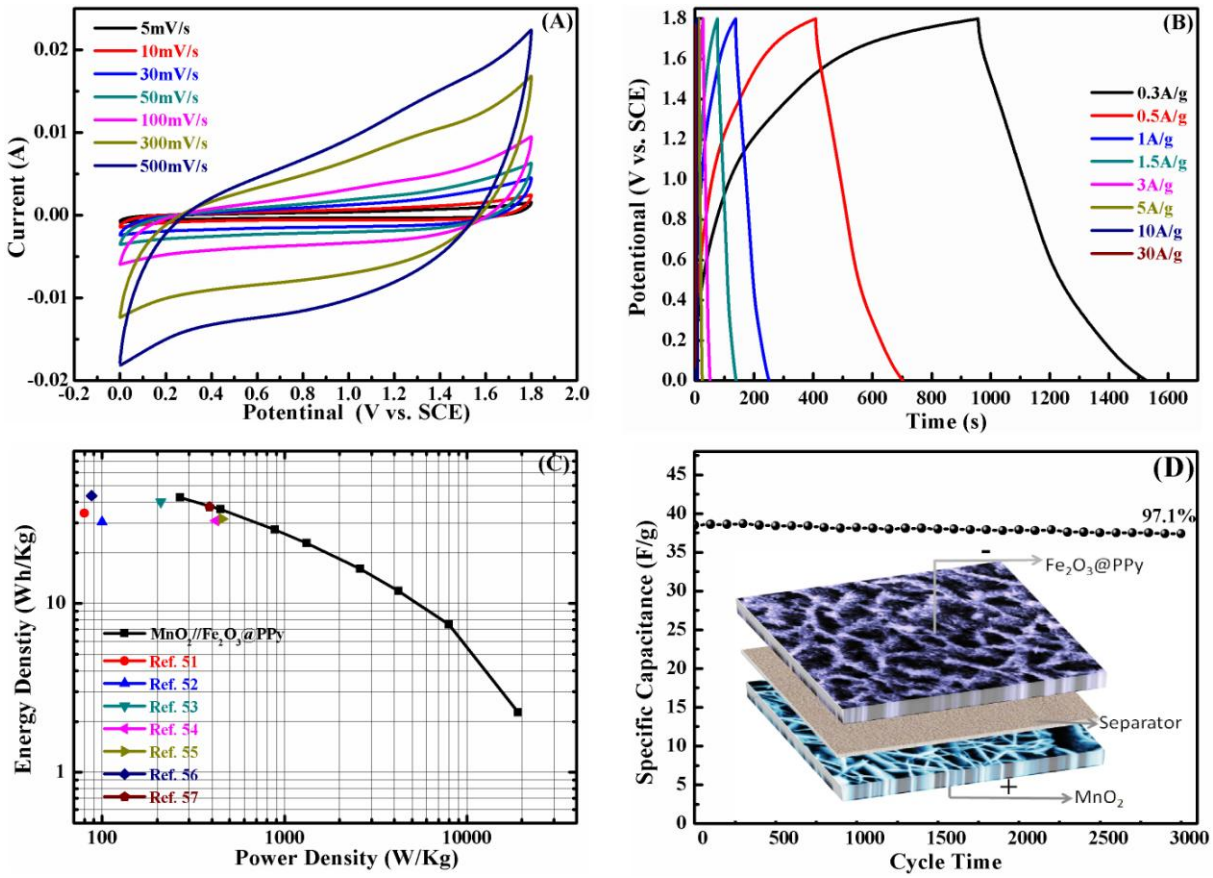

Figure 5. Electrochemical properties of bi-metal oxides ASC: (A) CV curves at different scan rates, (B) the GCD curves at different current densities, (C) the Ragone plot, (D) the life cycle stability at a current density of 3 A g^{-1} (the schematic of the ASC device shown in the inset).

To further testify the potential applications for energy storage device, a bi-metal oxides ASC device was assembled (as shown in the inset of Figure 5D, detail information see experimental section) based on the electrochemical results of Figure S11 and S12A with the MnO_2 nanosheets and the core-branch Fe_2O_3@PPy-0.3C electrodes as the positive electrode and negative electrode, respectively. The as-prepared bi-metal oxide ASC exhibits an ideal capacitive behavior with approximately rectangular CV curves from 5 to 500 mV s^{-1} (Figure 5A) within a potential window of 1.8 V, indicating its excellent power characteristics [46]. Moreover, the GCD curves

of the supercapacitor device at various current densities illustrated in Figure 5B maintain a good symmetry even at a high current density of 30 A g^{-1}, demonstrating its good rate capability. After deducted the IR drop (see Figure S12B), the obtained specific capacitance and volumetric capacitance of ASC at various current densities are shown in Figure S12C. And the corresponding calculated Ragone plot in Figure 5C reveals that the bi-metal oxides ASC delivers an energy density as high as 42.4 Wh kg^{-1} at a power density of 268.8 W kg^{-1} and maintains 2.3 Wh kg^{-1} at an extremely high power density of 19140 W kg^{-1}, which exhibits superior performance over Co_3O_4/PPy/MnO_2//AC (34.3 Wh kg^{-1} at 80.0 W kg^{-1}) [51], MnO_2 nanowire/graphene//graphene (30.4 Wh kg^{-1} at 100 W kg^{-1}) [52], graphitic hollow carbon spheres/MnO_2//graphitic hollow carbon spheres (40.0 Wh kg^{-1} at 210 W kg^{-1}) [53], $Ni(OH)_2$/graphene//reduced Hummers' graphene oxide (31 Wh kg^{-1} at 420 W kg^{-1}) [54], MnO_2-graphene foam//CNT-graphene (31.8 Wh kg^{-1} at 453.6 W kg^{-1}) [55] and CoO/PPy//AC (43.5 Wh kg^{-1} at 87.5 W kg^{-1}) [56] with graphene or AC as negative electrodes and is even higher than MnO_2//γ-FeOOH bi-metal oxides ASC (37.4 Wh kg^{-1} at 388.5 W kg^{-1}) [57]. Furthermore, the supercapacitor possesses long-term stability over 3000 cycles at a current density of 3 A g^{-1} as shown in Figure 5D. The specific capacitance of the device retains 37.4 F g^{-1} after 3000 cycles, corresponding to 97.1% of its initial specific capacitance (38.1 F g^{-1}), higher than MnO_2 nanowire/graphene//graphene (79% after 1000 cycles) [52], iron/graphene sheets//$Ni(OH)_2$/CNTs (78% after 2000 cycles) [29] and previous reported iron oxides or hydroxide based electrodes shown in table S1. In order to validate this result, we further performed SEM analysis of the core-branch Fe_2O_3@PPy after 3000 cycles (Figure S13). It is clear that core-branch Fe_2O_3@PPy still retains the honeycomb-like structure with randomly distributed PPy nanoleaves on the wall, revealing the protective shell PPy can tolerate the volume expansion and contraction of the Fe_2O_3

backbone during the cycle test. Besides, as displayed in Figure S14, a simple ASC device is presented to drive a mini-motor (1.5V, 22.5 mW) for approximately 15 s after charged at 5 A g^{-1} for 11s, demonstrating its potential for practical application.

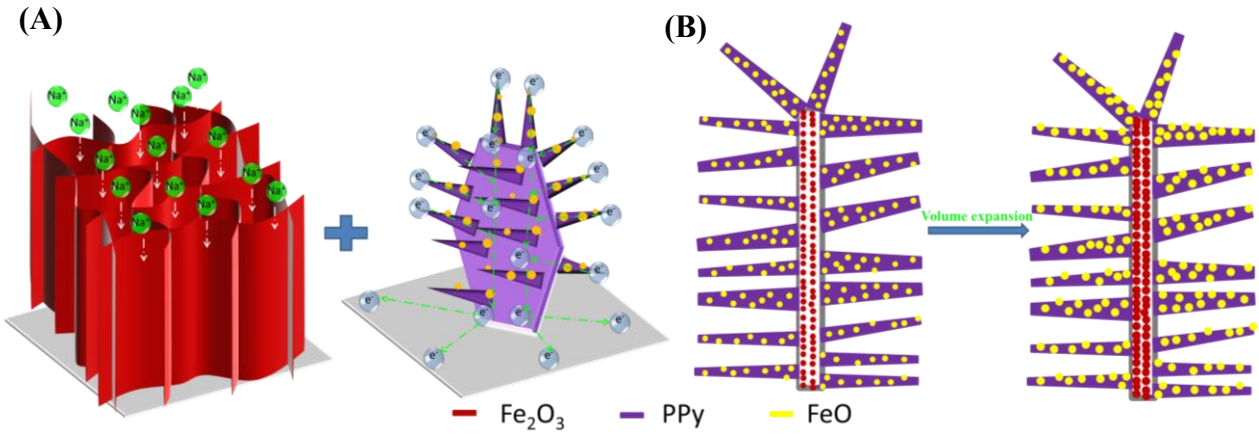

Schematic 2. The schematic representation of the electrolyte ion and electron transportation path (A) and volume change (B) during cycle.

The overall performances of the assembled supercapacitor using 3D core-branch Fe_2O_3@PPy-0.3C as negative electrode is superior to those with 0D (nanoparticles), 1D (nanotubes or nanorods), 2D (nanosheets), nanocomposites or core-shell structures in table S1, which could be attributed to the following structure merits: (i). the formation of honeycomb-like Fe_2O_3 backbone provides large contact area between the active material and the electrolyte (as shown in the left part of Schematic 2A), resulting in more efficient electrolyte ions transportation and greatly increment of material utilization efficiency; (ii). the wrapped PPy branch has superior electrical conductivity than Fe_2O_3 species, which could works as "superhighways", as illustrated in the right part of Schematic 2A. This core-branch structure leads to the fact that electrons can transport more efficiently during charge-discharge processes, and thus large improvement in specific capacitance; (iii). the excellent cycling stability of the obtained supercapacitor device using core-branch Fe_2O_3@PPy as negative electrode materials could be due to the strong

synergistic effect of honeycomb-like mesoporous Fe_2O_3 nanoflakes and PPy nanoleaves. Specifically, the mesoporous feature of honeycomb-like Fe_2O_3 nanoflakes [36] and the protective function of branched PPy nanoleaves prevent drastic volume variation of Fe_2O_3 and FeO nanoparticles during the electrolyte ions insertion/extraction process, [16, 37-38] which thus together improve the life cycle, as displayed in Schematic 2B.

Conclusion

In summary, this work constitutes a novel strategy to rationally design a core-branch honeycomb-like mesoporous Fe_2O_3 nanoflakes@PPy nanoleaves negative electrode by combing hydrogen bubbles dynamic template, hydrothermal method and electrochemical polymerization. The as-prepared core-branch Fe_2O_3@PPy electrode exhibits a large variety of unique physical and chemical properties, such as large accessible surface area, high chemical stability and much improved electrochemical performance. Moreover, the formation mechanism and morphogenesis evolution of branched PPy nanoleaves on honeycomb-like Fe_2O_3 nanoflakes have been elucidated to extract design principles that may enable the conductive polymer formation on other metal oxides with similar capabilities. Based on this advancement, a bi-metal oxides ASC device comprised of core-branch Fe_2O_3@PPy and MnO_2 nanosheets electrodes with a maximum energy density of 42.4 Wh kg^{-1} and a maximum power density of 19.14 kW kg^{-1} was achieved, with more than 97.1% capacitance retention after 3,000 cycles, which is easy to scale up to industrial production and holds great promise in energy storage/conversion devices.

Abbreviations

AC, activated carbon; CNTs, carbon nanotubes; PEDOT, poly (3,4-ethylenedioxythiophene); 3-D, three-dimensional; EDS, energy dispersive X-ray spectroscopy; SDS, sodium dodecyl sulfate;

Py, pyrrole; α-Fe_2O_3, Hematite; PPy, polypyrrole; NF, nickel foam; XRD, X-ray diffraction; XPS, X-ray photoelectron spectroscopy; SEM, scanning electron microscopy; TEM, transmission electron microscopy; HRTEM, high-resolution TEM ; HAADF, high angle annular dark field; EELS, electron energy loss spectroscopy; SCE, saturated calomel electrode; CV, cyclic voltammetry; GCD, galvanostatic charge-discharge; ASCs, asymmetrical supercapacitors.

Acknowledgements

We acknowledge the funding from Generalitat de Catalunya 2014 SGR 1638, 2014 SGR 797 and MINECO coordinated projects between IREC and ICN2 TNT-FUELS and e-TNT (MAT2014-59961-C2-2-R). Xuan Zhang is grateful for financial support from China Scholarship Council.

Appendix A. Supplementary Material

Supplementary material associated with this article can be found in the online version at http://dx.doi.org××××××.

References

[1] P. Simon, Y. Gogotsi, Nat. Mater. 7 (2008) 845-854.

[2] G. P. Wang, L. Zhang, J.J. Zhang, Chem. Soc. Rev. 41 (2012) 797-828.

[3] Y.W. Zhu, S. Murali, M.D. Stoller, K.J. Ganesh, W.W. Cai, P.J. Ferreira, A. Pirkle, R.M. Wallace, K.A. Cychosz, M. Thommes, D. Su, E.A. Stach, R.S. Ruoff, Science, 332 (2011) 1537-1541.

[4] A. Chu, P. Braatz, J. Power Sources, 112 (2002) 236-246.

[5] J. Jiang, Y.Y. Li, J.P. Liu, X.T. Huang, C.Z. Yuan, X.W.D. Lou, Adv. Mater., 24 (2012) 5166-5180.

[6] Y. X. Zeng, Y. Han, Y. T. Zhao, Y. Zeng, M.H. Yu, Y.J. Liu, H.L. Tang, Y.X. Tong, X.H. Lu, Adv. Energy Mater., 5 (2015) 1402176.

[7] L.Y. Yuan, X.H. Lu, X. Xiao, T. Zhai, J.J. Dai, F.C. Zhang, B. Hu, X. Wang, L. Gong, J. Chen, C.G. Hu, Y.X. Tong, J. Zhou, Z.L. Wang, ACS Nano, 6 (2011) 656-661.

[8] K. Jost, D.P. Durkin, L.M. Haverhals, E.K. Brown, M. Langenstein, H.C.D. Long, P. C. Trulove, Y. Gogotsi, G. Dion, Adv. Energy Mater. 5 (2015) 1401286.

[9] X.H. Lu, Y.X. Zeng, M.H. Yu, T. Zhai, C.L. Liang, S.L. Xie, M.S. Balogun, Y.X. Tong, Adv. Mater. 26 (2014) 3148-3155.

[10] Z.Y. Jin, A.H. Lu, Y.Y. Xu, J.T. Zhang, W.C. Li, Adv. Mater., 26 (2014) 3700-3705.
[11] J. Gamby, P. Taberna, P. Simon, J. Fauvarque, M. Chesneau, J. Power Sources, 101 (2001) 109-116.
[12] S. Park, M. Vosguerichian, Z.N. Bao, Nanoscale, 5 (2013) 1727-1752.
[13] M.F. El-Kady, V. Strong, S. Dubin, R.B. Kaner, Science, 335 (2012) 1326-1330.
[14] F. Bonaccorso, L. Colombo, G.H. Yu, M. Stoller, V. Tozzini, A.C. Ferrari, R.S. Ruoff, V. Pellegrini, Science 347 (2015) 6217.
[15] Z. Tang, C.H. Tang, H. Gong, Adv. Funct. Mater., 22 (2012) 1272-1278.
[16] M.F. Shao, Z.H. Li, R.K. Zhang, F.Y. Ning, M. Wei, D.G. Evans, X. Duan, Small, 11 (2015) 3530-3538.
[17] X.H. Lu, M.H. Yu, G.M. Wang, Y.X. Tong, Y. Li, Energy Environ. Sci., 7 (2014) 2160-2181.
[18] Z. Chen, Y.C. Qin, D. Weng, Q.F. Xiao, Y.T. Peng, X.L. Wang, H.X. Li, F. Wei, Y.F. Lu, Adv. Funct. Mater., 19, (2009) 3420-3426.
[19] T. Zhai, X.H. Lu, H.Y. Wang, G.M. Wang, T. Mathis, T.Y. Liu, C. Li, Y.X. Tong, Y. Li, Nano Lett., 15 (2015) 3189-3194.
[20] P.C. Chen, G.Z. Shen, Y. Shi, H.T. Chen, C.W. Zhou, ACS Nano,4 (2010) 4403-4411.
[21] J. Chang, M.H. Jin, F. Yao, T.H. Kim, V.T. Le, H.Y. Yue, F. Gunes, B. Li, A. Ghosh, S.S. Xie, Y.H. Lee, Adv. Funct. Mater., 23, (2013) 5074-5083.
[22] J. Xu, Q.F. Wang, X.W. Wang, Q.Y. Xiang, B. Liang, D. Chen, G.Z. Shen, ACS Nano, 7 (2013) 5453-5462.
[23] Q.T. Qu, S.B. Yang, X.L. Feng, Adv. Mater., 23 (2011) 5574-5580.
[24] X. Chen, K.F. Chen, H. Wang, D.F. Xue, Mater. Focus, 4 (2015) 78-80.
[25] S. Shivakumara, T.R. Penki, N. Munichandraiah, ECS Electrochem. Lett., 2 (2013) A60-A62.
[26] F. Meng, S.A. Morin, J. Song, J. Am. Chem. Soc., 133 (2011) 8408-8411.
[27] L.F. Chen, Z.Y. Yu, X. Ma, Z.Y. Li, S.H. Yu, Nano Energy, 9 (2014) 345-354.
[28] C. Guan, J.L. Liu, Y.D; Wang, L. Mao, Z.X. Fan, Z.X. Shen, H. Zhang, J. Wang, ACS Nano, 9, (2015) 5198-5207.
[29] C.L. Long, T. Wei, J. Yan, L.L. Jiang, Z.J. Fan, ACS Nano, 7 (2013) 11325-11332.
[30] H.T. Sharifi, E. Gracia-Espino, H.R. Barzegar, X.E. Jia, F. Nitze, G.Z. Hu, P. Nordblad, C.W. Tai, T. Wagberg, Nat. Commun., 4 (2013) 2319.
[31] H.W. Wang, Z.J. Xu, H. Yi, H.G. Wei, Z.H. Guo, X.F. Wang, Nano Energy, 7 (2014) 86-96.
[32] C.W. Cheng, H.J. Fan, Nano Today, 7 (2012) 327-343.
[33] W.W. Zhou, C.W. Cheng, J.P. Liu, Y.Y. Tay, J. Jiang, X.T. Jia, J.X. Zhang, H. Gong, H.H. Hng, T. Yu, H.J. Fan, Adv. Funct. Mater., 21 (2011) 2439-2445.
[34] R.R. Zamani, M. Ibáñez, M. Luysberg, N.G. Castelló, L. Houben, J.D. Prades, V. Grillo, R.E. Dunin-Borkowski, J.R. Morante, A. Cabot, J. Arbiol, ACS Nano, 8, (2014) 2290-2301.
[35] H.B. Li, A.G. Kanras, L. Manna, *Acc. Chem. Res.*, 46 (2013) 1387-1396.
[36] X.Z. Yu, B.A. Lu, Z. Xu, Adv. Mater., 26 (2014) 1044-1051.
[37] K. Liang, T.L. Gu, Z.Y. Cao, X.Z. Tang, W. C. Hu, B.Q. Wei, Nano Energy, 9 (2014) 245-251.
[38] H.J. Tang, J.Y. Wang, H.J. Yin, H.J. Zhao, D. Wang, Z.Y. Tang, Adv. Mater., 27 (2015) 1117-1123.

[39] A. Fakhry, F. Pillier, C. Debiemme-Chouvy, J. Mater. Chem. A, 2 (2014) 9859-9865.
[40] A. Fakhry, H. Cachet, C. Debiemme-Chouvy, Electrochimica Acta, 179 (2015) 297-303.
[41] D.W. Liu, Q.F. Zhang, P. Xiao, B.B. Garcia, Q. Guo, R. Champion, G.Z. Cao, Chem. Mater., 20 (2008) 1376-1380.
[42] D.W. Liu, B.B. Garcia, Q.F. Zhang, Q. Guo, Y.H. Zhang, S. Sepehri, G.Z. Cao, Adv. Funct. Mater., 19 (2009) 1015-1023.
[43] G.X. Gao, L. Yu, H.B. Wu, X.W. Lou, Small, 10 (2014) 1741-1745.
[44] Y. Yang, Z.W. Peng, G. Wang, G.D. Ruan, X.J. Fan, L. Li, H.L. Fei, R.H. Hauge, J.M. Tour, ACS Nano, 8, (2014) 7279-7287.
[45] M.V. Reddy, T. Yu, C.H. Sow, Z.X. Shen, C.T. Lim, G.V.S. Rao, B.V. R. Chowdari, Adv. Funct. Mater., 17, (2007) 2792-2799.
[46] X.H. Xia, D.L. Chao, X.Y. Qi, Q.Q. Xiong, Y.Q. Zhang, J.P. Tu, H. Zhang, H.J. Fan, Nano Lett., 13 (2013) 4562-4568.
[47] Q. Li, Z.L. Wang, G.R. Li, R. Guo, L.X. Ding, Y.X. Tong, Nano Lett., 12 (2012) 3803-3807.
[48] X. Yang, J. Zhu, L. Qiu, D. Li, Adv. Mater., 23 (2011) 2833-2838.
[49] X. Zhang, W. Shi, J. Zhu, D.J. Kharistal, W. Zhao, B.S. Lalia, H.H. Hng, Q. Yan, ACS Nano, 5, (2011) 2013-2019.
[50] J.B. Han, Y.B. Dou, J.W. Zhao, M. Wei, D.G. Evans, X. Duan, Small, 9 (2012) 98-106.
[51] L.J. Han, P.Y. Tang, L. Zhang, Nano Energy, 7 (2014) 42-51.
[52] Z.S. Wu, W. Ren, D.W. Wang, F. Li, B. Liu, H.M. Cheng, ACS Nano, 4 (2010) 5835-5842.
[53] Z. Chen, V. Augustyn, J. Wen, Y.W. Zhang, M.Q. Shen, B. Dunn, Y.F. Lu, Adv. Mater., 23 (2011) 791-795.
[54] H.L. Wang, Y.Y. Liang, T. Mirfakhrai, Z. Chen, H.S. Casalongue, H.J. Dai, Nano Res., 4 (2011) 729-736.
[55] Z.Y. Zhang, F. Xiao, L.H. Qian, J.W. Xiao, S. Wang, Y.Q. Liu, Adv. Energy Mater., 4 (2014) 1400064.
[56] C. Zhou, Y.W. Zhang, Y.Y. Li, J.P. Liu, Nano Lett., 13 (2013) 2078-2085.
[57] Y.C. Chen, Y.G. Lin, Y.K. Hsu, S.C.K. Yen, H. Chen, L.C. Chen, Small, 10 (2014) 3803-3810.

Vitae

Peng Yi Tang graduated in chemical engineering and technology at Hunan Normal University with a bachelor degree. And then he received a master degree of science in Lanzhou University in 2013 in China. In 2015, he started his PhD at Catalan Institute of Nanoscience and Nanotechnology (ICN2), CSIC and The Barcelona Institute of Science and Technology (BIST) in the Group of Advanced Electron Nanoscopy (GAe-N) under the supervision of Professor Jordi Arbiol at ICN2 and is co-directed by Professor Joan Ramon Morante from IREC on Advanced Electron Nanometrology Tools for Atomic Characterization of Energy Nanomaterials.

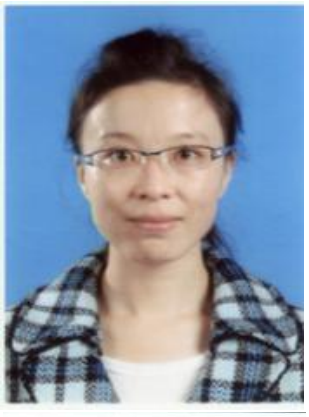

Li Juan Han received her MSc. degree from Lanzhou University in 2013 in China. Afterwards, she joined Professor Li Zhang's group in the Chinese University of Hong Kong (CUHK) as Research Assistant from 2013 to 2015. Now she is a Ph.D. candidate in Professor JR Galán-Mascarós's group in the institute of Chemical Research of Catalonia (ICIQ). Her current research interests lie in the fabrication of cost-effective water splitting catalysts for solar to fuel energy conversion.

Dr. Aziz Genç obtained his BSc and MSc degrees in Materials Science and Engineering from Yildiz Technical University and Istanbul Technical University, respectively. In 2015, he obtained his PhD at ICN2 and ICMAB-CSIC in the Group of Advanced Electron Nanoscopy (GAe-N) under the supervision of Prof. Jordi Arbiol. His main research activities span over the characterization of nanomaterials via transmission electron microscopy related techniques with an emphasis on the electron energy-loss spectroscopy.

Dr. Yong Min He received his Ph.D. degree in condensed state physics from Lanzhou University in 2015. He was supported by China Scholarship Council for eighteen months to carry out 2D material research studies at Rice University in October 2013 as a complimentary scholar. From 2015 to the present, he has been working in Nanyang Technological University of Singapore as a postdoctoral fellow. His current research interests are mainly focusing on "smart" flexible ECs, and two-dimensional (2D) materials such as graphene, hBN, transition metal dichalcogenides (TMDCs), and their heterostrucutre.

Xuan Zhang is pursuing a Ph.D. degree in the Department of Materials Engineering at KU Leuven under the supervision of Prof. Jan Fransaer. He obtained his BSc and MSc degrees in Physical Chemistry from Lanzhou University. His current research in surface and interface engineered materials group focuses on synthesis and characterization of carbon-metal oxide composite electrode materials for lithium-ion battery, supercapacitor and fuel cell.

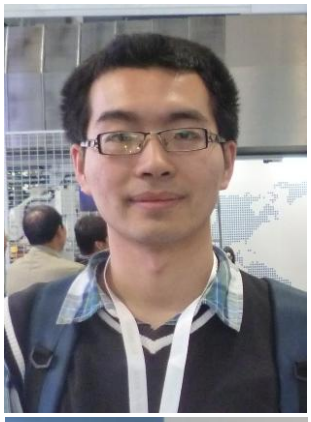

Lin Zhang obtained his B.Sc and M.Sc degrees in Mechanical Science and Engineering from Jilin University in 2011 and 2014, respectively. In 2015, he joined Dr. Allen Yi's group as a Ph.D. candidate. His main research activities span over the ultra-precision manufacturing and its applications on supercapacitor devices.

Prof. "JR" Galán-Mascarós received his PhD from University of Valencia, working in the group of Prof. E. Coronado. After a post- doctoral stay with Prof. Kim R. Dunbar at Texas A&M University, he went back to University of Valencia as a Research Fellow (Ramon and Cajal program). Currently, he is an ICREA research professor at the Institute of Chemical Research of Catalonia (ICIQ), which he joined in 2009. He is interested in the application of coordination chemistry in such different fields as solar fuels, energy applications, materials science and biomimetic catalysis.

Prof. Joan Ramon Morante received his PHD from University of Barcelona in 1980. He is full professor of the Faculty of Physics, University of Barcelona and director of the Catalonian Institute for Energy Research, IREC. His activities were centred in electronic materials and devices; semiconductors and electronics ceramics. He was also involved on nanomaterials for sensors, actuators and Micro and Nano systems, especially on chemical sensors. He is now focussed on “nano energy” addressing effort to the energy transfer mechanisms in solid interfaces involving electrons, photons and phonons as well as chemicals and photoelectrochemical processes. He has taken part in many R&D EU projects (>30) as well as in private industrial projects. He has co-authored more than 600 works in international

specialized journals with more of 13800 citations, several proposal patents (15) and he has been advisor of more than 35 PhD students; he is member of international committees and editorial boards of scientific journals. He has been general chairman of international events and has been guest editor of many special issues. He has been awarded the Narcís Monturiol of the Generalitat of Catalunya, and the "senior research distinction" of the Generalitat of Catalunya. Actually, he was also vice president of the European Materials Research Society.

Prof. Jordi Arbiol graduated in Physics at Universitat de Barcelona (UB) in 1997, where he also obtained his PhD (European Doctorate and PhD Extraordinary Award) in 2001 in the field of transmission electron microscopy (TEM) applied to nanostructured materials. He was Assistant Professor at UB. From 2009 to 2015 he was Group Leader at Institut de Ciència de Materials de Barcelona, ICMAB-CSIC. Since 2013 he is Vice-President of the Spanish Microscopy Society (SME). Since 2015 he is the leader of the Group of Advanced Electron Nanoscopy at Institut Català de Nanociència i Nanotecnologia (ICN2), CSIC and The Barcelona Institute of Science and Technology (BIST). He has been awarded with the 2014 EMS Outstanding Paper Award, the EU40 Materials Prize 2014 (E-MRS), listed in the Top 40 under 40 Power List (2014) by The Analytical Scientist and the PhD Extraordinary Award in 2001 (UB).